

Analysis of transients for binary mixture convection in cylindrical geometry

Kristina Lerman, David S. Cannell, and Guenter Ahlers

Department of Physics and Center for Nonlinear Science, University of California at Santa Barbara, Santa Barbara, California 93106

(Received 8 September 1998)

We present experimental results for early transients near the onset of convection of an ethanol-water mixture in cylindrical containers heated from below. The separation ratio of the mixture was $\psi \approx -0.08$, and the aspect ratios $\Gamma \equiv r/d$ (r is the radius and d the height of the sample cell) of two different containers were 10.91 and 11.53. For this system the onset of convection occurs via a subcritical Hopf bifurcation to traveling waves. Beyond the bifurcation we found transient radially traveling waves whose amplitude grew in time. We decomposed the transient patterns into azimuthal modes of the form $\cos m\theta$. The azimuthal symmetry of the pattern depended strongly on Γ . For $\Gamma = 10.91$ odd azimuthal modes were preferred, while for $\Gamma = 11.53$ even modes dominated. We measured the spatial and temporal growth rates at various $\epsilon \equiv \Delta T/\Delta T_c - 1$ for different azimuthal modes and compared the results for the two aspect ratios. We found the temporal growth rates to be proportional to ϵ , but the spatial growth rates were essentially independent of ϵ . Reflection coefficients deduced from the spatial growth rates agree with theory reasonably well. As convection evolved, the patterns collapsed onto one or more diameters, during which time higher-order azimuthal modes grew significantly in amplitude. [S1063-651X(99)06403-X]

PACS number(s): 47.54.+r, 47.20.Ky, 47.27.Te, 47.20.Bp

I. INTRODUCTION

A thin, quiescent horizontal layer of fluid heated from below is unstable to the formation of macroscopic flow patterns. The instability is a result of competition between the buoyancy forces experienced by the warmer, less dense fluid near the bottom and the dissipative effects of thermal conduction and viscosity. The control parameter that measures the external stress due to the temperature difference, the Rayleigh number, is defined as

$$R \equiv \frac{\alpha g \Delta T d^3}{\kappa \nu}. \quad (1)$$

Here $\alpha = -\rho^{-1}(\partial\rho/\partial T)_{P,c}$ is the thermal expansion coefficient at constant pressure P and mass concentration (weight fraction) c , ρ is the density, g is the acceleration due to gravity, κ and ν are the thermal diffusivity and kinematic viscosity, respectively, and ΔT is the temperature difference between the bottom and top of the fluid layer. In an infinitely extended horizontal layer of pure fluid of thickness d , the initial instability occurs when the Rayleigh number exceeds its critical value $R_c = 1708$ [1]. The collective motion of the warmer rising fluid and cooler falling fluid organizes into rolls [2,3]. The wavelength λ of the pattern at onset, the roll-pair size, is about twice the layer height. The refractive-index variation associated with the temperature variation which is induced by the fluid flow can be detected by optical means and used to visualize the pattern [4].

In binary-fluid mixtures, such as ethanol and water, the temperature and concentration fields are coupled through the Soret effect, so that an externally applied temperature gradient drives a mass flux. This results in a vertical concentration gradient which, in the presence of gravity, can stabilize or destabilize the quiescent fluid layer. Consequently, in addition to the Rayleigh number, there is a further dimensionless control parameter, the separation ratio ψ , defined as

$$\psi \equiv -\frac{\beta}{\alpha} S_T \bar{c} (1 - \bar{c}). \quad (2)$$

Here $\beta = \rho^{-1}(\partial\rho/\partial c)_{P,T}$ is the solutal expansion coefficient, S_T is the Soret coefficient, and \bar{c} is the mean concentration. In ethanol-water mixtures at reasonable operating temperatures, ψ can take on moderately negative or positive values which depend on the concentration. When ψ is positive (negative), then the concentration gradient is destabilizing (stabilizing). In addition to the Soret effect, the Dufour effect describes the heat flux generated by a concentration gradient, but it is extremely small in liquids and can be ignored.

The existence of a second control parameter leads to an array of interesting states and dynamic patterns not observed in pure-fluid convection [5]. In mixtures with sufficiently negative ψ , the bifurcation from the conduction state is a subcritical Hopf bifurcation to a time-dependent state of traveling waves. A variety of nonlinear structures have been observed in narrow rectangular and annular cells, including localized pulses of traveling-wave convection that coexist with quiescent fluid over a range of the Rayleigh number [6,7], and ‘‘dispersive chaos’’ [8–10] (a regime characterized by persistent erratic growth and decay of convection).

Previous experimental work on binary-fluid convection in a two-dimensional system with cylindrical geometry revealed a complex sequence of transients [11,12]. The first convection patterns seen above onset consist of radially inward- and outward-traveling rolls. When the temperature difference across the fluid layer is kept fixed, the rolls localize azimuthally into bands of nonlinear convection along one or more diameters of the cell. There the amplitude becomes very large, while it remains small elsewhere in the cell. The focused line(s) of convection then collapse radially to form a localized structure of convection near the cell center, surrounded by quiescent fluid. This structure often is a long-lived pulse, similar to the stable localized pulses of TW con-

vection observed in one-dimensional systems [6,7,13]. Subsequent evolution of the nonlinear transient depends strongly on the composition of the mixture [14].

Theoretical efforts aimed at understanding binary-fluid convection have primarily focused on use of the complex Ginzburg-Landau equation. This approach has qualitatively described the behavior of patterns with one spatial degree of freedom [5,15,16]. There exists a body of experimental [17–19] and theoretical [20,21] work on the subject of small amplitude (linear) transients of convection in negative separation-ratio mixtures in narrow rectangular cells. It was shown [18,22] that at onset, the convection amplitude can be decomposed into right- and left-traveling waves (TW's). The amplitudes of both TW's grow exponentially as the waves travel across the cell and the waves are reflected with loss by the end walls. This behavior is similar to that which we observe for cylindrical containers, with the waves propagating radially inward and outward and reflecting at the cell periphery.

A linear stability analysis for convection of a binary mixture in cylindrical geometry was carried out by Mercader *et al.* [23]. They studied the case of insulating sidewalls, which is not the case for our experimental arrangement, but they used fluid parameters quite close to our experimental ones. They found linear eigenfunctions in the form of spirals which rotate in the direction such that the arms trail. Because of reflection symmetry about the midplane, they find that clockwise rotating right-handed spirals and counterclockwise rotating left-handed spirals are degenerate. Consequently superpositions of such spirals are equally valid eigenfunctions. Such a superposition, which the authors refer to as a standing wave (it is standing in the azimuthal but not in the radial direction), varies azimuthally as $\cos m\theta$. The superposition results in convection rolls which travel both radially outward and radially inward, as demonstrated by Fig. 6(b) of Ref. [23]. In fact, the figure reveals the existence of a nearly pure standing wave (in the radial sense) at the cell center. This results from the superposition of inward- and outward-traveling waves of nearly equal amplitude. The figure also shows that the incoming waves are smaller in amplitude than the outgoing ones near the cell periphery, but that they grow in amplitude, relative to the outgoing ones, as they propagate inward radially. Their analysis also shows that for an aspect ratio close to our experimental ones the critical Rayleigh numbers for the onset of modes with different azimuthal mode numbers m can be nearly identical. Finally, they also find solutions in the form of wall modes in which the convection rolls propagate azimuthally, while the cell center is free or nearly free of convection. For our fluid parameters they find the critical Rayleigh number for such a wall mode to lie about 0.8% above those for the cell-filling spiral modes of low azimuthal wave number.

In this paper we present the results of a study of the effect of aspect ratio on the linear transients in a 25.0 wt % ethanol-water mixture, in cylindrical geometry, with a separation ratio $\psi \approx -0.08$. For this purpose we used two cells, one with a radial aspect ratio (radius/height) $\Gamma = 10.91$ and the other with $\Gamma = 11.53$. We find that the linear transient consists of radially outward- and inward-traveling waves, and that the wave amplitude varies azimuthally as $\cos m\theta$. Thus we observe a pattern that corresponds to the superposition state

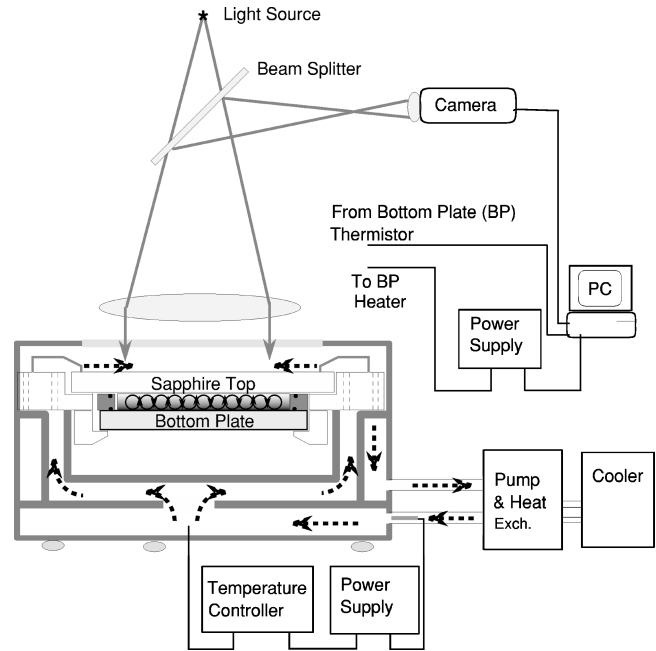


FIG. 1. Schematic diagram of the apparatus showing the convection cell, temperature-controlling bath, and shadowgraph apparatus. The arrows indicate the flow of temperature-controlled water used to maintain the sapphire top plate at constant temperature.

found by Mercader *et al.* [23]. We find that several low-order azimuthal modes are usually present simultaneously, even quite near threshold. For $\Gamma = 10.91$ these modes are predominantly odd, while for $\Gamma = 11.53$ even- m modes dominate. The simultaneous presence of several azimuthal modes is explained by the fact that the critical Rayleigh numbers for small m are very similar [23]. For the one aspect ratio they studied, $\Gamma = 11$, Mercader *et al.* found the $m = 1$ and $m = 3$ modes to have lower critical Rayleigh numbers than those of low-order even- m modes. This is consistent with our finding that even or odd modes are preferred for a given aspect ratio. We have never observed pure individual spirals, which may indicate that some selection mechanism is operable, even in the linear regime. On some occasions we have found spiral-like patterns with strong azimuthal variation, such as would result from a superposition of two opposite-handed spirals of unequal amplitude. Such a pattern can be seen as the first image of Fig. 9. Finally, we have not observed wall states, although we have not made any systematic search for them.

The remainder of this paper consists of five sections. Section II describes the apparatus, mixture preparation and properties, and various experimental details. Section III is devoted to the quantitative analysis of the convection patterns. Spatial and temporal evolution of the traveling-wave amplitude associated with each independent azimuthal mode are studied by fitting solutions of a simplified amplitude equation in cylindrical geometry [24] to the spatial and temporal profiles of the waves. Decomposition of the patterns into azimuthal modes enabled us to follow the evolution of each mode independently. Results for the two aspect-ratio cells during the linear transients are presented in Sec. IV. Section V provides a brief description of the nonlinear evolution following the initial linear transient for each aspect-ratio cell.

TABLE I. Experimental parameters describing the mixtures.

c	T_{mean} (°C)	d (cm)	Γ	κ (cm ² /s)	ν (cm ² /s)	σ	L	ψ	τ_v (s)
0.2504	20.539	0.362	10.91	0.00102	0.0247	24.12	0.0065	-0.0795	128.24
0.2501	20.946	0.343	11.53	0.00102	0.0243	23.74	0.0066	-0.0797	114.62

II. EXPERIMENTAL METHODS AND MATERIALS

A schematic diagram of the apparatus is shown in Fig. 1. The convection cell containing the fluid is located inside a stainless-steel can which is thermally insulated from the environment by means of a circulating temperature-controlled water bath. The convection cell itself consists of a sapphire top plate and a silver bottom plate separated by an annular Delrin spacer sealed to each plate by an O ring. The apparatus is optically accessible from above to enable shadowgraph observation of convection patterns. A typical convection apparatus of the type we used has been described in detail elsewhere [25–27].

The top plate is an optically flat single-crystal sapphire, 102 mm in diameter and 9.5 mm thick. The top surface of the sapphire is held at a fixed temperature to an accuracy of 1–2 mK by means of circulating water. The bottom plate is a 90-mm-diam silver plate 9.5 mm thick, diamond machined to a mirror finish. It has a 100 Ω resistive film heater attached to its lower surface, and two thermistors are embedded within it. The temperature of the silver plate is regulated to better than 0.1 mK stability. To minimize warping of the rather soft silver plate, the plate separation was monitored interferometrically during cell assembly.

Two annular Delrin sidewalls, both with an inner diameter of 7.90 cm and an outer diameter of 9.4 cm, were used. They had different thicknesses, $d=0.362$ cm and $d=0.343$ cm, resulting in radial aspect ratios $\Gamma=r/d=10.91$ and $\Gamma=11.53$, respectively. Each sidewall had an O ring groove on its top and bottom surfaces as well as two radial fill holes. The O rings were ethylene-propylene hydroxide cured, with a cross-sectional diameter of 0.119 cm. We used six cylindrical Delrin posts, set into the sidewalls, to fix the cell height. The height uniformity of the assembled cells was within $\pm 0.04\%$.

We used 200 proof ethanol and de-ionized filtered water for the mixture preparation. Mixtures were degassed by the ‘‘freeze, pump, thaw’’ method. The relevant experimental and fluid parameters for each sample are shown in Table I. Each fluid is identified by its alcohol concentration c and the aspect ratio of the cell Γ . The mean temperature given in the table was calculated as $T_{\text{mean}}=T_{\text{bath}}+\Delta T_c/2$. Literature data for the thermal diffusivity κ , Soret coefficient S_T , mass diffusivity D [28], density ρ , and shear viscosity η [29] were interpolated using polynomial fits to obtain $\nu=\eta/\rho$, the Prandtl number $\sigma=\nu/\kappa$, the Lewis number $L=D/\kappa$, and the separation ratio ψ . The polynomial fits to $\rho(c,T)$ were used to obtain the thermal and solutal expansion coefficients. The vertical thermal diffusion time $\tau_v=d^2/\kappa$ was used to scale experimental times, while lengths were scaled by the layer thickness d .

The shadowgraph apparatus was nearly identical to that

described in Ref. [26], and will not be described here. We found a good compromise between sensitivity and distortion by using the charge-coupled device (CCD) camera to image a plane corresponding to viewing the shadowgraph signal about 3 m from the cell. The camera signal was digitized to an 8-bit resolution at each pixel. The static nonuniformities in light intensity over the cell were removed from the image by dividing each image of convection, pixel by pixel, by a background image taken in the conduction state. For display purposes, but not during analysis, divided images were re-scaled so that the largest value was set to 255 (white on the 8-bit gray-scale used in display), and the smallest value was set to 0 (black).

The convective threshold was crossed quasistatically, by making small steps in ΔT and waiting for 3 h between steps. The experimental threshold $\epsilon\equiv\Delta T/\Delta T_c-1=0$ was defined to be halfway between the last point in the conduction regime and the first point at which convection was seen. Our step size in ΔT corresponded to $\Delta\epsilon\approx 0.0015$. In order to study linear transients for $\epsilon<0$, we allowed convection to grow at a supercritical ϵ , and then suddenly reduced the temperature difference to achieve a negative ϵ .

III. DATA ANALYSIS

At the onset of convection the azimuthal symmetry of the observed pattern was broken in a way that depended strongly on the aspect ratio of the cell. In all cases the rolls filled the cell and traveled radially, consistent with the circular geometry of the container, but the amplitude of convection varied in a way that was consistent with a superposition of modes having azimuthal variation of the form $\cos m\theta$. Here $m=0,1,2,\dots$, is a small integer. The dominant mode(s) depended sensitively on the aspect ratio. For $\Gamma=10.91$, for example, the dominant azimuthal modes were odd. Typical patterns seen at this aspect ratio were a superposition of $m=1$ [Fig. 2(a)] and $m=3$ [Fig. 2(b)] azimuthal modes. Modes with even m were suppressed in this geometry. The dashed circle drawn for reference in the image in Fig. 2(a) is concentric with the cell. The circle crosses the line of nodes, which is indicated by a dashed line. At the line of nodes the dark concentric part of each convection roll, corresponding to upflowing fluid, becomes light, indicating a region of downflowing fluid. If the aspect ratio is changed by a small amount $\approx 1/2$, azimuthal modes of even symmetry are favored at onset. Figures 2(c) and 2(d) illustrate patterns consisting primarily of a mixture of the $m=0$ and other even azimuthal modes seen in the $\Gamma=11.53$ cell. Odd modes were also present for this aspect ratio, but they were generally weaker. The presence of a number of azimuthal modes at the same time is indicative that the critical Rayleigh number is

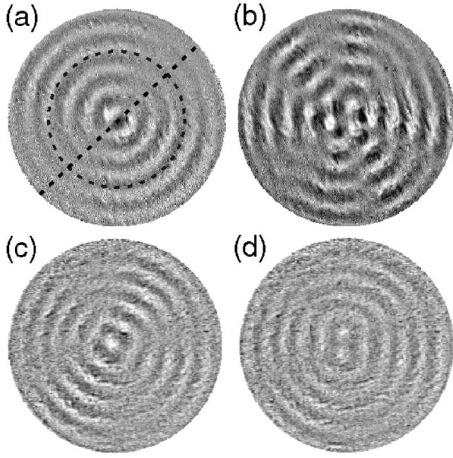


FIG. 2. Azimuthal modes at the onset of convection in two cells with slightly different aspect ratio. (a) and (b) are for $\Gamma = 10.91$, and (c) and (d) are for $\Gamma = 11.53$. The dominant azimuthal modes in (a) and (b) are the odd modes $m=1$ and $m=3$. In (c) and (d) even modes are dominant: image (c) is a mixture of $m=0$ and $m=4$, while in (d) $m=2$ dominates. In (a) the dashed circle, concentric with the cell wall, is drawn to bring out the phase change associated with the $m=1$ mode. The line of nodes is indicated by the dashed line.

nearly independent of the azimuthal mode number m . This is also consistent with the theoretical analysis of Mercader *et al.* [23] who found critical Rayleigh numbers for $m=1$ and $m=3$ differing by only 0.02%, for parameter values similar to those of our experiment.

These observations, together with the findings of Mercader *et al.* [23] and a simple, but physically insightful model, suggested by Cross [24], motivated us to analyze the data in the linear regime in terms of a superposition of various azimuthal modes of the form $\cos m\theta$. In this model the convection amplitude away from the cell center is expressed as

$$\sqrt{r}\Psi(r, \theta, t) = \text{Re} \left\{ \sum_m [A_m^+(r, t) e^{i(q_c r - \omega_c t)} + A_m^-(r, t) e^{-i(q_c r + \omega_c t)}] \cos(m\theta + \delta_m) \right\}, \quad (3)$$

where δ_m is an offset, A_m^+ and A_m^- are slowly varying amplitudes which refer to waves traveling radially outward and inward, respectively, and q_c and ω_c are the critical wave vector and angular frequency at onset, respectively. The \sqrt{r} factor is included explicitly to eliminate the natural asymptotic large- r dependence of waves in a cylindrical geometry, leaving only a slow variation to be captured by the amplitudes $A_m^\pm(r, t)$.

The amplitudes A^+ and A^- are assumed to satisfy linearized amplitude equations, as they do for pure-fluid convection in cylindrical geometry [30,31],

$$\tau_0 [\partial_t A^+(r, t) + s_0 \partial_r A^+(r, t)] = \tilde{\epsilon} A^+(r, t), \quad (4a)$$

$$\tau_0 [\partial_t A^-(r, t) - s_0 \partial_r A^-(r, t)] = \tilde{\epsilon} A^-(r, t), \quad (4b)$$

where τ_0 sets the time scale for pattern growth or decay, and s_0 is the group velocity of traveling waves at onset. No diffusion term is included in Eqs. (4) because it was shown to be unnecessary for capturing much of the observed behavior of linear traveling waves in one-dimensional cells [20,21]. The various parameters entering the model equations may be obtained to a good approximation by linear stability analysis of the laterally infinite system [32] and are summarized in Table II. In calculating these parameters we used ψ values chosen to reproduce the experimentally measured critical frequencies for the two samples, rather than the literature values corresponding to their concentrations and mean temperatures. The dimensionless critical angular frequencies were found to be 5.99 and 5.87 for the aspect ratio 10.91 and 11.53 cells, respectively. The linear-frequency-based ψ values were -0.085 for the 10.91 aspect ratio sample, and -0.082 for the 11.53 aspect ratio sample, as compared to the literature values of -0.0795 , and -0.0797 , respectively. The reader should also note the extreme sensitivity of the group velocity s_0 to ψ . A change of only 3.7% in ψ results in a 20% change in s_0 .

Within the context of this model, the traveling-wave amplitudes

$$A_m^+ = a_m^+ e^{\sigma_m t} e^{\lambda_m r} e^{i(q_m r - \Omega_m t)}, \quad (5a)$$

$$A_m^- = a_m^- e^{\sigma_m t} e^{-\lambda_m r} e^{-i(q_m r + \Omega_m t)} \quad (5b)$$

have exponential profiles in space, and grow (or decay) exponentially in time. Here σ_m and λ_m are the temporal and spatial growth rates, respectively, for mode m , a_m^+ and a_m^- may be complex to accommodate phase shifts, and q_m and Ω_m are small deviations from q_c and ω_c , respectively. The reader should note that we are using the term ‘‘spatial growth rate’’ for the inverse length scale λ_m , which characterizes the envelope of the linear-wave amplitude in the cell. It should not be confused with the ϵ -dependent ‘‘spatial growth rate’’ $\epsilon/s_0\tau_0$ that characterizes the growth in amplitude of a linear pulse of convection as it travels.

In order that the ansatz represented by Eqs. (5) satisfy Eqs. (4), the relationship $\tau_0\sigma + \tau_0s_0\lambda = \tilde{\epsilon}$ must hold. Onset will be observed experimentally when the temporal growth rate σ becomes positive. For finite aspect-ratio cells this occurs for a positive value of $\tilde{\epsilon}$ given by

TABLE II. Parameters obtained from the linear stability analysis.

c	Γ	ψ	R_c	k_c	s_0	τ_0	ξ_0^2
0.2504	10.91	-0.085	1879.6	3.1198	1.0544	0.10303	0.1477
0.2501	11.53	-0.082	1873.6	3.1198	0.8791	0.10305	0.1477

$$\tilde{\epsilon}_s(\Gamma) = -\frac{\tau_0 s_0}{2\Gamma} \ln \gamma. \quad (6)$$

Thus there is an onset shift which is linear in Γ^{-1} , as was found previously for the one-dimensional case [33,34]. For the one-dimensional system, this onset shift has been measured experimentally [35] and used to determine values for the reflection coefficient γ .

The striking resemblance of Eqs. (5) to the right- and left-traveling wave solutions of the linearized amplitude equation in one dimension [18–21] reveals the motivation for the model. In cylindrical geometry, the inward-traveling wave at θ becomes the outward-traveling wave at $\pi + \theta$, as the wave moves through the cell center. This process may also involve a phase shift which we denote by ϕ_c , and assume to be m independent. This implies

$$a_m^+ = (-1)^m a_m^- e^{i\phi_c}. \quad (7)$$

The waves are reflected by the wall at $r = \Gamma$, and the outward-traveling wave becomes the inward-traveling one. We denote the complex reflection coefficient by $\gamma e^{i\phi_r}$ and assume it also to be m independent. This results in the relationship

$$a_m^- = \gamma \exp[i\phi_r] a_m^+ \exp[2\lambda_m \Gamma] \exp[i2(q_c + q_m)\Gamma]. \quad (8)$$

Equations (7) and (8) in turn imply

$$\ln \gamma = -2\lambda_m \Gamma \quad (9)$$

and

$$\phi_c + \phi_r + 2(q_c + q_m)\Gamma = (2n - m)\pi, \quad (10)$$

where n is an integer.

Equation (9) indicates that, to within the accuracy of the model, the spatial growth rate λ_m should be m independent. It is also clear that, in the linear state, λ is determined by the modulus of the reflection coefficient γ and the aspect ratio Γ , and it should be independent of $\tilde{\epsilon}$.

Because onset will actually occur first for the mode(s) nearest the critical wave vector, i.e., with q_m as small as allowed by Eq. (10), it is clear that, as Γ is varied, even- and odd- m modes will be favored alternately at onset. The change in Γ necessary to go from favoring even to favoring odd m , or vice versa, is just $\Delta\Gamma = \pi/2(q_c + q_m) \approx 1/2$, because $q_c \approx \pi$, and $q_m \ll q_c$. Such behavior has been observed previously [36] in rectangular cells, and is well described by pairs of amplitude equations [33].

It is necessary to decompose the convection patterns into their azimuthal modes, in order to determine the temporal and spatial growth rates σ_m and λ_m for each mode. Figure 3 illustrates this process. The original image shown as Fig. 3(a) was sine and cosine transformed azimuthally with $m = 1, 3$ and 5 in this case. This served to determine the offsets δ_m . The data were then multiplied pixel by pixel by $\cos(\theta + \delta_m)$ and averaged azimuthally. For example, Fig. 3(b) shows the data of Fig. 3(a) multiplied by $\cos(\theta - 2.20)$. The azimuthal averaging eliminated all but a single m mode and, after multiplication by \sqrt{r} , produced a radial function $A_m(r, t_0) = \text{Re}[A_m^+(r, t_0)e^{i(q_c r - \omega_c t_0)} + A_m^-(r, t_0)e^{-i(q_c r + \omega_c t_0)}]$. This

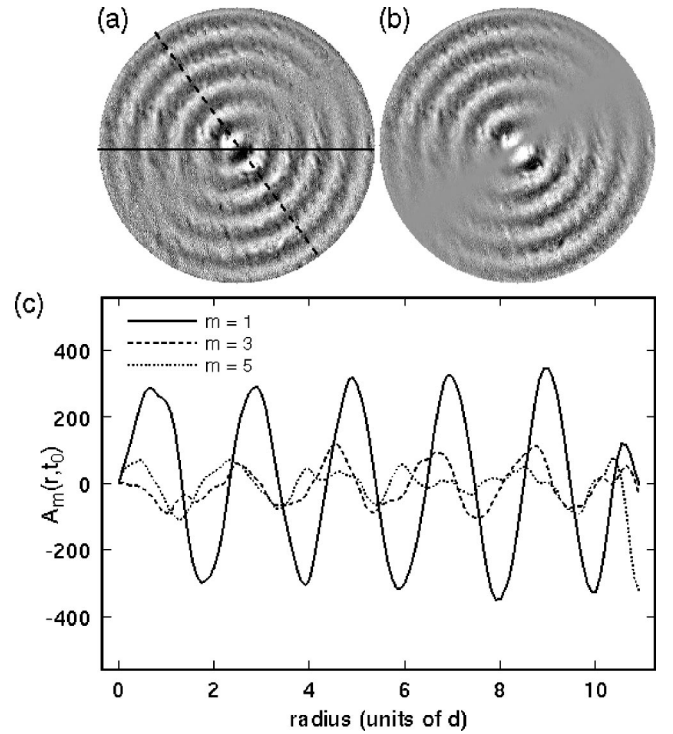


FIG. 3. Analysis of a pattern to determine the amplitude of the $m=1$ mode: The pattern in (a) is multiplied by $\cos(\theta - \delta_1)$ with $\delta_1 = 2.2$. The product, shown in (b), is azimuthally averaged, and the result, after multiplication by \sqrt{r} , is shown in (c). Results for other odd modes, $m=3$ and $m=5$, are also shown in (c). The solid line in (a) shows the axis from which θ is measured, and the dashed line indicates the azimuthal offset $\theta = \delta_1$ of the $m=1$ mode.

function is the sum of the outgoing and incoming wave amplitudes corresponding to the selected m at a given instant in time $t = t_0$ [see Eq. (3)]. It is shown in Fig. 3(c) for $m = 1, 3$, and 5. Clearly the pattern shown in Fig. 3(a) is dominated by the $m=1$ mode, and has only weak radial dependence remaining after allowing for $\Psi \propto 1/\sqrt{r}$. The weak radial dependence is consistent with the assumptions of the model.

We used Fourier demodulation to separate the radial function into outgoing and incoming waves. A time series of 256 successive determinations of $A_m(r, t)$ separated in time by a fraction of the vertical thermal diffusion time τ_v was measured. Such a series is best displayed as a gray-scaled space-time plot such as is shown in Fig. 4(a) for data taken in the $\Gamma = 10.91$ cell. Each horizontal line is a gray-scaled version of the measured $A_m(r, t)$ at a particular time, with successive measurements displaced upward along the time axis. In this case, the total time interval involved was $18.81\tau_v$. This representation reveals the presence of both outgoing and incoming waves. The waves are quite similar in amplitude near $r = 0$, giving rise to a deeply modulated standing wave. Near the outer boundary at $r = \Gamma$, the incoming wave is clearly much weaker than the outgoing one, as would be expected for a weakly reflecting boundary. The reader should note that the left half of Fig. 4(a) is the reflection of the right half about $r = 0$, and contains no additional information. We retain both halves to emphasize the similarity to convection in a one-dimensional container extending from $-\Gamma$ to $+\Gamma$. It does mean, however, that the “right”-traveling waves are outgoing in the right half of the space-time plot and incom-

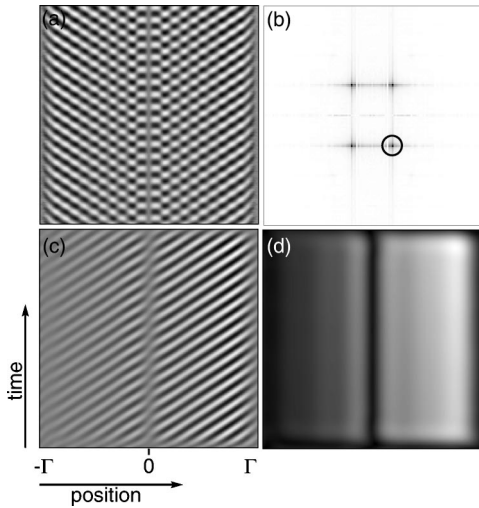


FIG. 4. Time-series analysis of the $m=1$ mode. (a) Gray-scaled image of a time series of 256 radial functions $A_1(r, t_i)$, for the $m=1$ mode in the $\Gamma=10.91$ cell for the same conditions as Fig. 3. (b) Central region of the Fourier-transform plane, enlarged by a factor of 2, showing the modulus of the transform. Performing the inverse Fourier transform after multiplication by a filter function centered on the circled peak, which corresponds to right TW's, leads to the time series for the right TW's shown in (c) and to their envelope shown in (d).

ing in the left half. The waves were separated into ‘‘right’’ and ‘‘left’’ TW's by Fourier transforming a space-time plot such as that of Fig. 4(a), using a filter which preserved only a single peak, and then inverting the transform. In order to implement the filter, the signal at each point (r, θ) of Fourier space was multiplied by a function of the form

$$[1 + \tanh(r-r_1)/w_r][1 + \tanh(r_2-r)/w_r] \\ \times [1 + \tanh(\theta-\theta_1)/w_\theta][1 + \tanh(\theta_2-\theta)/w_\theta].$$

The parameters r_1 and r_2 set the radial, and θ_1 and θ_2 the azimuthal, bounds of the filter. The parameters w_r and w_θ fix the sharpness of the cutoff in the radial and azimuthal directions, respectively. The results of this procedure are illustrated in Figs. 4(b) and 4(c). Figure 4(b) is a gray-scaled representation of the modulus of the Fourier transform of Fig. 4(a). Image 4(c) shows, also in gray scale, the real part of the inverse transform, with the filter centered on the peak circled in Fig. 4(b). The resulting time series of the ‘‘right’’ TW's show the steady growth in amplitude beginning after reflection at the left side of image 4(c), and continuing as the waves pass through the cell center. Figure 4(c) also reveals a significant phase shift as the waves cross $r=0$.

A signal proportional to the envelope of the right TW's is obtained as the modulus of the inverse transform which is shown in Fig. 4(d). The signal amplitude has been artificially forced to zero at $r=0$, by the \sqrt{r} factor, resulting in the vertical black stripe in the center of Fig. 4(d) and the low-amplitude regions visible in the centers of Figs. 4(a) and 4(c). A horizontal cut through image 4(d) gives the spatial dependence of the TW envelope at a fixed time. The left-hand half corresponds to radially incoming waves and the right-hand half to outgoing waves. A vertical cut at a fixed position reveals the temporal behavior of the right TW's.

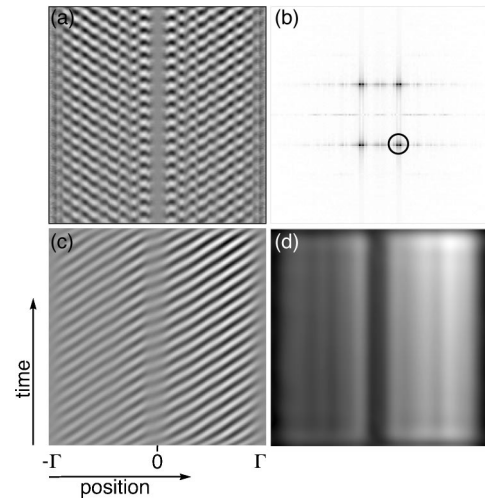


FIG. 5. Time-series analysis of the $m=3$ mode. (a) Gray-scaled image of a time series of 256 radial functions $A_3(r, t_i)$, for the $m=3$ mode in the $\Gamma=10.91$ cell for the same conditions as Fig. 3. (b) Central region of the Fourier-transform plane, enlarged by a factor of two, showing the modulus of the transform. Performing the inverse Fourier transform after multiplication by a filter function centered on the circled peak, which corresponds to right TW's, leads to the time series for the right TW's shown in (c) and to their envelope shown in (d). Note the relatively larger region of low amplitude near $r=0$ as compared to Fig. 4.

Thus a vertical cut on the left half shows the growth or decay of incoming waves with time and on the right half that of outgoing waves.

Figure 5 shows examples of the same type of analysis for the $m=3$ mode as that presented in Fig. 4 for the $m=1$ mode. The most obvious difference is the larger region of small amplitude near $r=0$. The width of this region increased with m , as might be expected for waves having a nonzero correlation length in the direction parallel to the rolls. Again a significant phase shift is visible in Fig. 5(c) as the waves cross the center.

For each run, several series of 256 images, each series covering a period of about $20\tau_v$, were collected. Such measurements were begun about $20\tau_v$ after the last change in ϵ . Time scans at two fixed locations and spatial scans at two fixed times were extracted from the time series data for each cell. For the $\Gamma=10.91$ cell, the time scans were extracted at $r_0=\pm 6.5d$. The spatial scans for this cell were extracted starting at times $t_1=2\tau_v$ and $t_2=14\tau_v$, as measured from the beginning of each time series. The spatial scans were averaged over a period $\Delta t=3\tau_v$. For the $\Gamma=11.53$ cell, the time scans were extracted at $r_0=\pm 6.8d$. The spatial scans were extracted starting at times $t_1=3\tau_v$ and $t_2=17\tau_v$, and they were averaged over a time $\Delta t=3\tau_v$. The temporal averaging of the data for the spatial scans was done to reduce the effects of small scratches in the bottom plate.

Figure 6 shows examples of such scans both in time, Fig. 6(a), and in space Fig. 6(b), for the $m=1$ mode in the $\Gamma=10.91$ cell. These scans were extracted from the time series shown in Fig. 4(d). In this run convection was allowed to grow for $\approx 84\tau_v$ at $\epsilon=2.3\times 10^{-3}$, after which time the control parameter was reduced to $\epsilon=-1.53\times 10^{-3}$. Even at this negative ϵ , the strong convection pattern evident in Fig. 3

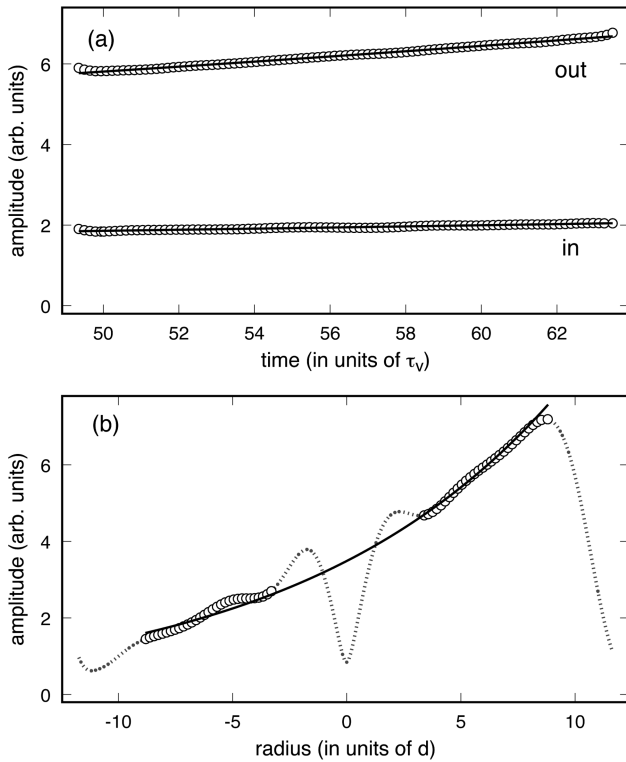


FIG. 6. Analysis of the temporal and spatial growth of the $m = 1$ mode. (a) Two scans at fixed radial positions $r = \pm 6.5d$, showing the temporal evolution of the incoming and outgoing TW's in the $\Gamma = 10.91$ cell. (b) Line scan (averaged over a period $2\tau_v$) showing the spatial profile of the right TW's from Fig. 4(d) at a fixed time. The solid lines represent single-exponential fits to the data. In (b) only the points away from the cell center and side walls (represented by circles) are fitted.

continued to grow, and the pattern eventually became non-linear before dying out some time later. Data from this run were not used for the purposes of measuring linear growth rates, but the strong convection patterns are useful to illustrate the method of analysis.

The lines marked in (out) in Fig. 6(a) refer to ingoing (outgoing) waves. For the spatial scan shown in Fig. 6(b) it is obvious that there are regions both near the cell center and at the wall where the amplitude decays rather abruptly. The decay near $r = 0$ is the result of multiplication by \sqrt{r} together with the effects of filtering described above; the actual wave amplitude is large near the cell center. Data from these regions are indicated by dots and were excluded from the fits discussed below.

To obtain the temporal growth rate σ_m of mode m , we fit the time scan by a single exponential of the form $c + D_m \exp(\sigma_m t)$, with D_m and σ_m adjustable. The small constant offset term c was fixed at 0.010, the value obtained from a time series of images without convection. This background comes from various sources: camera noise, light scattered from scratches in the bottom plate, and nonuniformities in the cooling bath flow. In fitting the data, the time t was taken as the time from the last change in ϵ , and thus D_m represents the amplitude at the time of that change. We fit only the central 192 of the 256 points to reduce the edge artifacts associated with the Fourier transform and demodu-

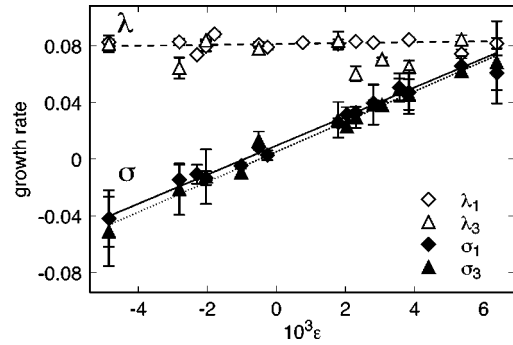


FIG. 7. Spatial (λ) and temporal (σ) growth rates as a function of ϵ for the $m = 1$ and $m = 3$ modes in the $\Gamma = 10.91$ cell. The straight lines are fits to the data. The dashed line is a single fit to the combined spatial growth-rate data for λ_1 and λ_3 , and the solid and dotted lines are the fits to the temporal growth rates, σ_1 and σ_3 , respectively.

lation of a finite image. Temporal growth rates of both the outgoing and the incoming waves were measured and were identical to within our accuracy, as would be expected. The solid lines in Fig. 6 are the exponential fits to the data.

Spatial scans were also fit by an exponential $c + F_m \exp(\lambda_m r)$ with the same constant background offset. F_m and λ_m were adjusted to give the spatial growth rates λ_m of the modes. The spatial profiles are fit reasonably well by single exponentials, provided data near the walls and in the vicinity of the cell center are excluded from the fit. The solid line in Fig. 6(b) is the result of a single-exponential fit to the portion of the data shown as open circles. The spatial growth rates λ_m , especially those for weaker modes, were harder to measure and showed more variability than did the temporal growth rates σ_m .

The spatial profiles of the TW envelopes of all azimuthal modes display the same characteristics independent of ϵ . They all have a roughly exponential shape over most of the cell, excluding regions close to the center of the cell and a small distance from the side walls. In these healing regions, the amplitude of the rolls decreases rapidly. The healing length is approximately one roll pair (one wavelength) in extent. This is consistent with studies of traveling waves in narrow rectangular cells [22]. These features — exponential growth, the shape and length of healing regions — are generally insensitive to the details of Fourier demodulation, in particular to the size and sharpness of the region of Fourier space that is retained by the filter for demodulation.

IV. RESULTS AND DISCUSSION

We used the procedure described above to measure the temporal and spatial growth rates of different azimuthal modes as a function of ϵ in the two different aspect ratio cells. Temporal and spatial growth rates of the strongest modes in the $\Gamma = 10.91$ cell are plotted versus ϵ in Fig. 7. The amplitude of the linear TW grows in time at a rate proportional to the distance from threshold, $\sigma = \epsilon/\tau_0$. The spatial growth rates, on the other hand, show little dependence on ϵ . This is consistent with the model. The various straight lines represent fits of the form $y = a + b\epsilon$ to the data. For example, the temporal growth rate of the $m = 1$ mode gives

TABLE III. Results of linear fits of the form $y = a + b\epsilon$, to the spatial and temporal growth rates of different azimuthal modes in two different aspect ratio cells, together with the reflection coefficients γ obtained from the spatial growth rates.

m	a_{σ_m}	b_{σ_m}	a_{λ_m}	b_{λ_m}	γ
$\Gamma = 10.91$					
1	0.0095 ± 0.0009	10.26 ± 0.46	0.0812 ± 0.0004	0.32 ± 0.15	0.170 ± 0.002
3	0.0052 ± 0.0023	10.65 ± 0.70	0.0786 ± 0.0006	-1.83 ± 0.24	0.180 ± 0.002
$\Gamma = 11.53$					
0	0.0025 ± 0.0010	9.89 ± 0.37	0.082 ± 0.002	0.46 ± 0.58	0.151 ± 0.007
2	0.0036 ± 0.0016	10.24 ± 0.40	0.078 ± 0.002	-0.14 ± 0.41	0.164 ± 0.006
4	-0.0033 ± 0.0029	10.07 ± 0.81	0.086 ± 0.003	-3.98 ± 0.84	0.139 ± 0.010

$a_{\sigma_1} = 0.0095 \pm 0.0009$, and $b_{\sigma_1} = 10.3 \pm 0.45$. These coefficients, and similar results for $m=3$, are collected in Table III. The fits pass through zero at $\epsilon = -a/b = -(9 \pm 1) \times 10^{-4}$ for the $m=1$ mode and $-(5 \pm 2) \times 10^{-4}$ for the $m=3$ mode. Thus, to within the uncertainty of ± 0.0008 associated with the experimental threshold determination, the temporal growth rates vanish at the point where $\epsilon=0$. The time scale for this mixture is $\tau_0 = 0.103$; therefore, the slope of the temporal growth rates, the inverse of τ_0 , is expected to be 9.71. This agrees reasonably well with the experimental results of 10.3 ± 0.5 and 10.6 ± 0.7 . Fits to the spatial growth rates of the $m=1$ and 3 modes are also given in Table III. They provide no evidence of an ϵ dependence.

Growth rates of different azimuthal modes in the $\Gamma = 11.53$ aspect-ratio cell, at different values of ϵ , are shown in Fig. 8. Again the temporal growth rates are linearly dependent on ϵ , and the spatial growth rates are independent of ϵ . The coefficients derived from linear fits for $m=0, 2$, and 4 are also given in Table III. Temporal growth rates vanish at $\epsilon = -a/b = -(3 \pm 1) \times 10^{-4}$ and $-(4 \pm 2) \times 10^{-4}$ for the strongest modes. Again this is within the ± 0.0008 experimental resolution of the convection threshold. The coefficients derived from fits to the spatial growth rates can be found in Table III as well. These results are also consistent with λ_m being independent of ϵ . Moreover, all the fits collectively suggest that the temporal growth rates of all azimuthal modes in the two geometries evolve in the same manner with respect to ϵ .

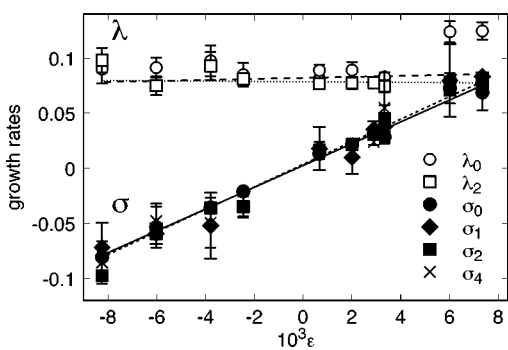


FIG. 8. Spatial (λ) and temporal (σ) growth rates as a function of ϵ for various modes in the $\Gamma = 11.53$ cell. The dashed and dotted straight lines are fits to the spatial growth-rate data for λ_0 and λ_2 , respectively. The solid and short dashed lines are fits to the temporal growth-rate data for σ_0 and σ_2 , respectively.

Because the gain in amplitude corresponding to passage across the cell is balanced by reflection loss, the modulus of the reflection coefficient, γ_m , is related to the spatial growth rate λ_m and aspect ratio: $\gamma_m = \exp[-2\lambda_m\Gamma]$. Thus, we may use our results for the spatial growth rates of various modes in the two different geometries to obtain values for γ_m . The results are also collected in Table III. The average values for $\Gamma = 10.91$ ($\Gamma = 11.53$) are $\gamma = 0.175$ ($\gamma = 0.151$), with no clear dependence on m . Physically, the value of the reflection coefficient depends on the ratio of thermal properties of the fluid and the walls, as well as on the lateral distance by which the walls extend beyond the fluid [33]. Analytic [33] and numerical [37] investigations of the ψ dependence of the reflection coefficient predicted that for small enough separation ratios, $\gamma \propto \sqrt{|\psi|}$. However, experiments that used the onset shift to determine the reflection coefficient in narrow rectangular samples [35] found that over a wide range of negative ψ , γ was constant and approximately 0.33. This value is about 50% higher than the theoretical [33,37,35] value of 0.23 appropriate to the conditions of those experiments. For our experiments the ratio of the sidewall thermal conductivity to that of the fluid was 0.5. The ratio of the sidewall thermal diffusivity to that of the fluid was 1.1, and our sidewalls extended 3.9 thermal penetration lengths beyond the fluid. Consequently our experimental conditions are very close to those of curve (c) Fig. 2(a) of Ref. [37], which gives a theoretical reflectivity of 0.17 for $\psi = -0.08$. Our results for γ are in the range 0.14–0.18, and thus agree rather well with the theoretical prediction. The most obvious difference between our experiment and previous reflectivity measurements [35,38] is the presence of sidewalls in the rectangular geometry, which are absent in the circular geometry.

V. NONLINEAR TRANSIENTS

As the amplitude of convection grew, the linear state always gave way to a nonlinear one. During this evolution, higher m azimuthal modes became detectable, and their amplitudes increased faster than did the amplitudes of the lower m modes. Simultaneously, convection became localized along one or more diameters of the cell. This focusing process is illustrated by the sequence of images in Fig. 9 taken at $\epsilon = -1.0 \times 10^{-3}$ in the $\Gamma = 10.91$ cell. The images in Fig. 9 are indexed by time from the onset of convection, in units of τ_v . The linear transient was allowed to grow at $\epsilon = 2.8 \times 10^{-3}$. The first image in the figure, at $t = 70.6\tau_v$, was

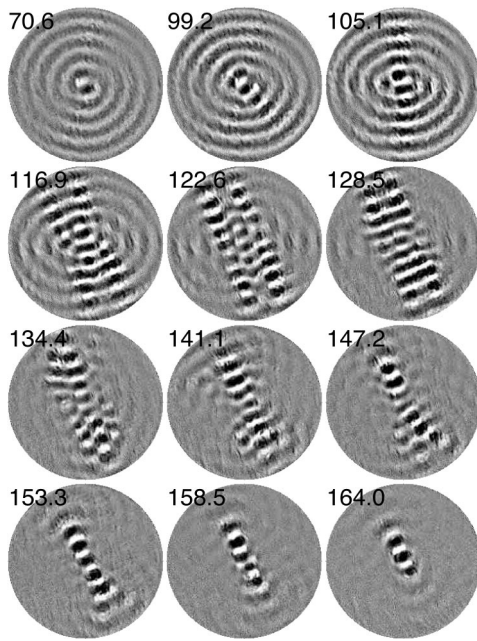


FIG. 9. Evolution of nonlinear transients in the $\Gamma = 10.91$ cell showing azimuthal focusing. The images are labeled by the elapsed time since the onset of convection, in units of τ_v . Linear transients were initially allowed to evolve at $\epsilon = 2.8 \times 10^{-3}$. Shortly after the first image in the figure was taken, the control parameter was reduced to $\epsilon = -1.0 \times 10^{-3}$. Subsequent images were taken at this value of ϵ .

taken during the linear transient, when $m=1$ was the dominant mode of the pattern. Shortly after this image was taken, the control parameter was reduced to a value below threshold, $\epsilon = -1.0 \times 10^{-3}$. At this negative value of ϵ the evolution of nonlinear transients proceeded in a manner very similar to their behavior at positive ϵ . Azimuthal focusing had become quite pronounced by around $t = 120\tau_v$, by which time the convection amplitude was localized in a broad double stripe along the diameter of the cell. With time, this stripe continued to narrow, eventually forming a single band of convection slightly before $t = 150\tau_v$. This band of convection began to shrink away from the wall, thereby forming a long pulse. Depending on ϵ , this second stage of collapse resulted in a radially localized pulse of convection, very similar to the ones studied in one-dimensional cells [7,6], or a localized but disordered region of convection, which, in 25% mixtures, grew to fill the cell with a steady state of stationary overturning convection [12,14]. During the process of forming a localized pulse the TW frequency, measured near the cell center, gradually decreased to about $2/3$ of the linear (Hopf) frequency.

The time evolution of the outgoing wave amplitude of the three strongest azimuthal modes is shown in Fig. 10. These amplitudes were computed from time series of images using the techniques described previously. The scans for $50\tau_v < t < 70\tau_v$ show the evolution of the linear transients at $\epsilon = 2.8 \times 10^{-3}$. During this time the pattern is dominated by the $m=1$ mode, although all three modes have nearly equal temporal growth rates. After ϵ was decreased to a negative value, at time $75\tau_v$, all of the modes continued to grow, with the $m=5$ mode doing so quite dramatically.

Figure 11 shows another example of the evolution of the

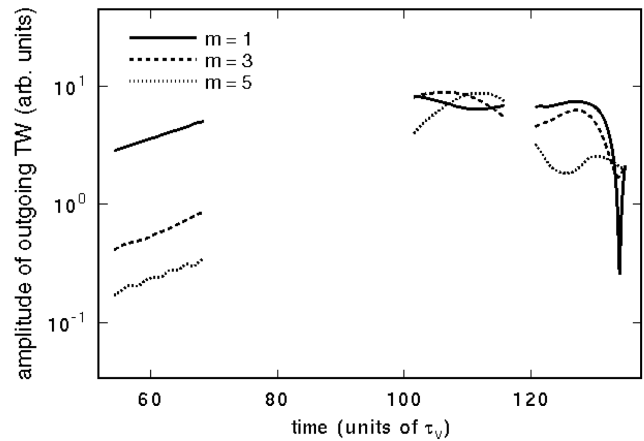


FIG. 10. Amplitudes of the outgoing traveling waves of the three strongest azimuthal modes in the $\Gamma = 10.91$ cell as a function of time elapsed since the onset of convection. The data shown for times between $50\tau_v$ and $70\tau_v$ were taken in the linear regime at $\epsilon = 2.8 \times 10^{-3}$, with all modes having comparable temporal growth rates, although differing considerably in amplitude. The control parameter was reduced to $\epsilon = -1.0 \times 10^{-3}$ around $75\tau_v$. Note the remarkable increase in the amplitudes of the $m=3$ and $m=5$ modes, following the reduction in ϵ . This growth corresponds to the azimuthal focusing process shown in Fig. 9.

nonlinear transient in the $\Gamma = 10.91$ cell. This run, conducted at $\epsilon = 3.8 \times 10^{-3}$, illustrates the infrequent case in which the $m=3$ mode was dominant in the linear regime. Convection localized azimuthally along the three diameters of the cell corresponding to the angular locations where the $m=3$ mode was strongest. After some time, convection along all three

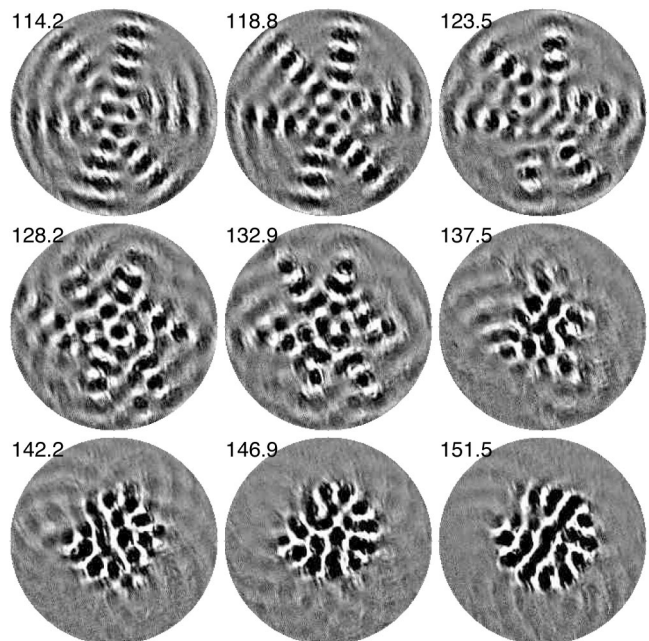


FIG. 11. Nonlinear-transient evolution in the $\Gamma = 10.91$ cell at $\epsilon = 3.8 \times 10^{-3}$. Images are indexed by time since the onset of convection, in units of τ_v . The $m=3$ mode evolves into a nonlinear convection state involving three bands of convection localized along cell diameters, and this pattern subsequently collapses radially to form a disorganized ‘blob’ of convection.

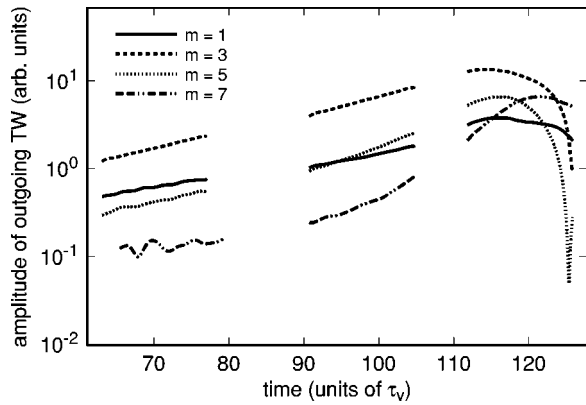


FIG. 12. Amplitudes of the outgoing traveling waves associated with four different azimuthal modes in the $\Gamma=10.91$ cell at $\epsilon=3.8 \times 10^{-3}$ as a function of time since the onset of convection.

diameters collapsed away from the wall, leading to a localized but disorganized “blob” of convection near the center of the cell. During this process the traveling-wave frequency fell to about $1/3$ of the Hopf frequency. The traveling-wave frequency dropped to zero a few hours later, when the cell filled with stationary convection rolls. Similar experiments using a mixture with nearly the same separation ratio, but different alcohol concentrations revealed similar behavior in the linear regime, but rather different nonlinear evolution [14].

Figure 12 shows the amplitude of the outgoing traveling waves for the four strongest azimuthal modes. For times before $80\tau_v$, that is, during the linear regime, the pattern is dominated by the $m=3$ mode, although the three strongest modes have comparable growth rates. Focusing starts around $90\tau_v$. After this time, the amplitudes and the growth rates of all modes increase, but those of the two highest modes, $m=5$ and $m=7$, increase more rapidly. For the period $60\tau_v-80\tau_v$ the growth rates are $\sigma_1=0.0328$, $\sigma_3=0.0467$, $\sigma_5=0.0446$, and $\sigma_7=0.0180$, while for the time

period $90\tau_v-110\tau_v$ the growth rates are $\sigma_1=0.0400$, $\sigma_3=0.0527$, $\sigma_5=0.0715$, and $\sigma_7=0.0917$. The tendency of the higher azimuthal modes to grow at much faster rates than the lower ones seems to be a generic feature of the nonlinear regime.

VI. CONCLUSION

A decomposition method for describing TW transients in binary fluid convection in cylindrical geometry has been presented and used to study transients in two different aspect-ratio cells. The symmetries of the patterns are found to depend sensitively on aspect ratio. For $\Gamma=10.91$, odd- m azimuthal modes of the form $\cos m\theta$ were selected at the onset of convection while the even modes were very weak. For $\Gamma=11.53$, on the other hand, even- m modes, including $m=0$, were dominant, and the odd- m modes were suppressed. The analysis gives results for the spatial and temporal behavior of the slowly varying envelopes of the ingoing and outgoing waves associated with each azimuthal mode. We found that the temporal growth rates of the strongest modes in both aspect ratio cells vanished at the experimental onset of convection, and varied linearly with ϵ . The spatial growth rates of all modes, on the other hand, were found to be independent of ϵ . The time evolution of individual azimuthal modes was followed well into the nonlinear regime. All modes exhibited comparable temporal growth rates, although differing in amplitude, during the linear transient regime. During the nonlinear period higher m azimuthal modes grew faster, becoming comparable in amplitude to lower m modes. This corresponded to azimuthal focusing of rolls onto bands of convection lying along one or more diameters of the cell, a characteristic feature of the nonlinear regime.

ACKNOWLEDGMENTS

This work was supported by the National Science Foundation through Grant No. DMR94-19168. We gratefully acknowledge helpful conversations with M.C. Cross.

-
- [1] S. Chandrasekhar, *Hydrodynamic and Hydromagnetic Stability* (Oxford University Press, London, 1961).
- [2] A. Schlüter, D. Lortz, and F. Busse, *J. Fluid Mech.* **23**, 129 (1965).
- [3] For experimental results, see, for instance, Y. Hu, R. Ecke, and G. Ahlers, *Phys. Rev. E* **48**, 4399 (1993); and references therein.
- [4] Perhaps the first to use the shadowgraph method was P.L. Silveston, *Forsch. Geb. Ingenieurwes* **24**, 29 (1958); **24**, 59 (1958). For more modern accounts, see, for instance, F.H. Busse and J.A. Whitehead, *J. Fluid Mech.* **66**, 67 (1974); V. Steinberg, G. Ahlers, and D.S. Cannell, *Phys. Scr.* **32**, 534 (1985); D.R. Jenkins, *J. Fluid Mech.* **190**, 451 (1988); J.R. deBruyn, E. Bodenschatz, S. Morris, S. Trainoff, Y.-C. Hu, D.S. Cannell, and G. Ahlers, *Rev. Sci. Instrum.* **67**, 2043 (1996); S. Trainoff and D.S. Cannell (unpublished).
- [5] For a recent review, see for instance M.C. Cross and P.C. Hohenberg, *Rev. Mod. Phys.* **65**, 851 (1993).
- [6] E. Moses, J. Fineberg, and V. Steinberg, *Phys. Rev. A* **35**, 2757 (1987).
- [7] R. Heinrichs, G. Ahlers, and D.S. Cannell, *Phys. Rev. A* **35**, 2761 (1987).
- [8] P. Kolodner, J. Glazier, and H. Williams, *Phys. Rev. Lett.* **65**, 1579 (1990).
- [9] J. Glazier, P. Kolodner, and H. Williams, *J. Stat. Phys.* **64**, 945 (1991).
- [10] P. Kolodner, S. Slimani, N. Aubry, and R. Lima, *Physica D* **85**, 165 (1995).
- [11] E. Bodenschatz, D.S. Cannell, J.R. de Bruyn, R. Ecke, Y.-C. Hu, K. Lerman, and G. Ahlers, *Physica D* **61**, 77 (1992).
- [12] K. Lerman, E. Bodenschatz, D.S. Cannell, and G. Ahlers, *Phys. Rev. Lett.* **70**, 3572 (1993).
- [13] J. Niemela, G. Ahlers, and D.S. Cannell, *Phys. Rev. Lett.* **64**, 1365 (1990).
- [14] K. Lerman, G. Ahlers, and D.S. Cannell, *Phys. Rev. E* **53**, R2041 (1996).

- [15] O. Thual and S. Fauve, *Europhys. Lett.* **49**, 1829 (1988).
- [16] W. van Saarloos and P.C. Hohenberg, *Phys. Rev. Lett.* **64**, 749 (1990).
- [17] R.W. Walden, P. Kolodner, A. Passner, and C.M. Surko, *Phys. Rev. Lett.* **55**, 496 (1985).
- [18] P. Kolodner and C.M. Surko, *Phys. Rev. Lett.* **61**, 842 (1988).
- [19] P. Kolodner, C.M. Surko, and H.L. Williams, *Physica D* **37**, 319 (1989).
- [20] M.C. Cross and E.Y. Kuo, *Physica D* **59**, 90 (1992).
- [21] M.C. Cross, *Physica D* **37**, 315 (1989).
- [22] P. Kolodner and H. Williams, in *Nonlinear Evolution of Spatio-Temporal Structures in Dissipative Continuous Systems*, edited by F.H. Busse and L. Kramer (Plenum Press, New York, 1990).
- [23] I. Mercader, M. Net, and E. Knobloch, *Phys. Rev. E* **51**, 339 (1995).
- [24] M.C. Cross (private communication).
- [25] G. Ahlers, D.S. Cannell, L.I. Berge, and S. Sakurai, *Phys. Rev. E* **49**, 545 (1994).
- [26] J.R. deBruyn, E. Bodenschatz, S. Morris, S. Trainoff, Y.-C. Hu, D.S. Cannell, and G. Ahlers, *Rev. Sci. Instrum.* **67**, 2043 (1996).
- [27] M.A. Dominguez-Lerma, G. Ahlers, and D.S. Cannell, *Phys. Rev. E* **52**, 6159 (1995).
- [28] P. Kolodner, H. Williams, and C. Moe, *J. Chem. Phys.* **88**, 6512 (1988).
- [29] E. Lax and C. Synowietz, *Taschenbuch für Chemiker und Physiker* (Springer-Verlag, Berlin, 1967).
- [30] S.N. Brown and K. Stewartson, *Stud. Appl. Math.* **57**, 187 (1977).
- [31] S.N. Brown and K. Stewartson, *Proc. R. Soc. London, Ser. A* **360**, 455 (1978).
- [32] We are indebted to W. Hort and W. Schöpf for providing us with programs to carry out the linear stability analysis.
- [33] M.C. Cross, *Phys. Rev. Lett.* **57**, 2935 (1986).
- [34] P. Kolodner, A. Passner, C.M. Surko, and R.W. Walden, *Phys. Rev. Lett.* **56**, 2621 (1986).
- [35] E. Kaplan and V. Steinberg, *Phys. Rev. E* **48**, R661 (1993).
- [36] C.M. Surko and P. Kolodner, *Phys. Rev. Lett.* **58**, 2055 (1987).
- [37] M.S. Bourzutschky and M.C. Cross, *Phys. Rev. A* **45**, R8317 (1992).
- [38] P. Kolodner, C.M. Surko, A. Passner, and H.L. Williams, *Phys. Rev. A* **36**, R2499 (1987).